ANALYSIS OF A FINITE STATE COAXIAL ROTOR INFLOW MODEL

Yong-Boon Kong
kyongboo@gatech.edu

J. V. R. Prasad
jvr.prasad@ae.gatech.edu

School of Aerospace Engineering
Georgia Institute of Technology
Atlanta, Georgia, 30332, USA

Chengjian He
he@flightlab.com

Advanced Rotorcraft Technology, Inc.
Sunnyvale, CA 94085

Abstract

An Active-Receiving Rotor Inflow Model (ARRIM) developed from potential flow theory has been shown in the literature to predict experimentally observed coaxial rotor inflow and its impact on rotor power variation with rotor thrust in hover. However, discrepancies have been noticed between the coaxial rotor forward flight performance predictions based on inflow computed using ARRIM and experimental data. In order to gain further understanding of the reasons for the observed discrepancies, the present study is aimed at a detailed analysis of rotor inflow predictions from ARRIM and compare the results with a high fidelity simulation model. Towards this, the ARRIM is implemented in FLIGHTLAB® and its inflow distribution in forward flight is analyzed and compared with the inflow distribution obtained using the Vortex Particle Model from the literature. It is found that while the mean inflow predictions from the ARRIM and the Vortex Particle Model are somewhat similar, the fore-to-aft inflow gradient predictions are significantly different. At higher advance ratios, side-to-side inflow gradient differences are also found between the two models.

1. NOMENCLATURE

α_j^r, β_j^r	Inflow states corresponding to cosine and sine components
χ	Wake skew angle, $\tan^{-1}\left(\frac{\mu}{\lambda_f+\lambda_m}\right)$
λ_0, λ_{1c}, λ_{1s}	Uniform, first harmonic fore-to-aft and side-to-side induced inflow distribution
λ_f	Inflow due to free-stream
λ_m	Total induced inflow at rotor
μ	Advance ratio
ν, η, ψ	Ellipsoidal coordinates
$\vec{\nabla}$	Gradient operator
ϕ	Pressure potential
ψ	Azimuthal position on rotor disk
Ψ_n^m	Inflow shaping function
τ_n^{mc},τ_n^{ms}	Pressure coefficients of cosine and sine components
ξ	Streamline coordinates
C_T	Thrust coefficient
$[L]$	Influence coefficient matrix
M, N	Total number of harmonics and radial terms
m, r	Harmonic number
n, j	Polynominal number
$\bar{P}_n^m$, $\bar{Q}_n^m$	Normalized Legendre function of the first and second kind
$\bar{r}$	Radial position normalized with respect to rotor radius
t	Time
$\bar{v}_z$	Induced downwash normalized with respect to blade tip speed
$\vec{v}$	Perturbration velocity vector
V_∞	Free-stream velocity
$[V_m]$	Mass flow parameter

2. INTRODUCTION

For real-time rotorcraft simulations, the Peters-He finite state inflow model[1] provides an efficient and accurate means to calculate rotor inflow. Although the single rotor pressure potential finite state model has been used extensively in standard software such as FLIGHTLAB®[2] and RCAS[3], etc., the model is not applied to coaxial configurations due to lack of off-disk solutions.

The Active-Receiving Rotor Inflow Model (ARRIM) concept[4] was developed to address this issue by relating the pressure from an active rotor to induced inflow at a receiving rotor. The model after incorporating into RCAS was shown to correctly

predict total power required for the Harrington teetering coaxial rotor[5,6] in hover but underestimated power required during forward flight mode. While reasons for the discrepancy so far have been attributed to inability to capture the distortion effect of upper rotor wake at the lower rotor[7], a finite state model that can predict coaxial rotor inflow accurately is far from complete.

In order to better understand reasons for the mismatch between ARRIM power prediction and experimental data, a high-fidelity Vortex Particle Model[8,9] (VPM) is used to study the mutual flow interference between upper and lower rotors. The present work analyses the differences in coaxial rotor flow fields predicted by the VPM and those estimated by ARRIM. This allows for making appropriate corrections to ARRIM parameters in order to capture the complex rotor-to-rotor flow field interactions which are difficult to model using potential flow theory.

3. ACTIVE-RECEIVING INFLOW MODELING

ARRIM is formulated from continuity and momentum equations of an incompressible potential flow given as,

(1) $$\vec{\nabla} \cdot \vec{v} = 0$$

(2) $$\frac{\partial \vec{v}}{\partial t} - V_\infty \frac{\partial \vec{v}}{\partial \xi} = -\vec{\nabla}\phi$$

The on-disk inflow is modelled by using shaping functions, Ψ_n^m with associated cosine and sine harmonics and weighting coefficients.

(3) $$\bar{v}_z = \sum_r^M \sum_{j=r+1,r+3\ldots}^N \Psi_j^r(\nu)[\alpha_j^r \cos(r\psi) + \beta_j^r \sin(r\psi)]$$

(4) $$\Psi_j^r(\nu) = \frac{\bar{P}_j^r(\nu)}{\nu}$$

In addition, the pressure term ϕ, in equation (2) is expanded in terms of Legendre polynomials and harmonic functions.

(5) $$\phi = \sum_m^M \sum_{n=m+1,m+3\ldots}^N \bar{P}_n^m(\nu)\bar{Q}_n^m(\eta)[\tau_n^{mc}\cos(m\psi) + \tau_n^{ms}\sin(m\psi)]$$

By substituting equations (3) through (5) into equation (2) and assuming steady-state case, the relationship between inflow states and pressure coefficients can be obtained as,

(6) $$\begin{Bmatrix}\alpha_1\\ \alpha_2\end{Bmatrix} = [V_m]^{-1}\begin{bmatrix}L_{11} & L_{12}\\ L_{21} & L_{22}\end{bmatrix}_{\cos}\begin{Bmatrix}\tau_1^c/2\\ \tau_2^c/2\end{Bmatrix}$$

(7) $$\begin{Bmatrix}\beta_1\\ \beta_2\end{Bmatrix} = [V_m]^{-1}\begin{bmatrix}L_{11} & L_{12}\\ L_{21} & L_{22}\end{bmatrix}_{\sin}\begin{Bmatrix}\tau_1^s/2\\ \tau_2^s/2\end{Bmatrix}$$

In equation (6), α_1 and α_2 correspond to column vectors of cosine components of inflow states from upper (denoted as 1) and lower (denoted as 2) rotors, respectively. Similarly, β_1 and β_2 in equation (7) are column vectors of sine components of inflow states for upper and lower rotors, respectively. The pressure coefficients τ_1 and τ_2 are vector coefficients of pressure fields from upper and lower rotors, respectively. The subscripts "$\cos$" and "$\sin$" in the equations refer to influence coefficient matrix (L-matrix) corresponding to cosine and sine components. The diagonal blocks L_{11} and L_{22} relate self-induced inflow to the aerodynamic loading on each rotor which is the same as a single rotor Peters-He L-matrix. The off-diagonal blocks L_{12} and L_{21} relate the inflow coupling between the two rotors where the elements in each block are given in equations (8) through (13). The subscripts "1" and "2" in the equations refer to the upper and lower rotor coordinate systems, respectively. ARRIM assumes a rigidly skewed cylindrical wake geometry with contraction effects taken into account. This is done by using a wake contraction table indexed by wake skew angle to correct the streamline coordinates in equations (8) through (13). The wake table used in this study was derived using the velocity potentials of the Galerkin method based inflow model.

For the elements in $[L_{12}]$,

(8) $$L_{jn,\cos}^{0m} = \frac{1}{2\pi}\int_0^{2\pi}\int_0^1 \Psi_j^0(\nu_1) * \int_0^\infty \frac{\partial(\bar{P}_n^m(\nu_2)\bar{Q}_n^m(\eta_2)\cos(m\psi_2))}{\partial z_1} d\xi_2 d\nu_1 d\psi_1$$

(9) $$L_{jn,\cos}^{rm} = \frac{1}{\pi}\int_0^{2\pi}\int_0^1 \Psi_j^r(\nu_1)\cos(r\psi_1) * \int_0^\infty \frac{\partial(\bar{P}_n^m(\nu_2)\bar{Q}_n^m(\eta_2)\cos(m\psi_2))}{\partial z_1} d\xi_2 d\nu_1 d\psi_1$$

$$L^{rm}_{jn,\sin} = \frac{1}{\pi}\int_0^{2\pi}\int_0^1 \Psi^r_j(\nu_1)\sin(r\psi_1)* \int_0^\infty \frac{\partial(\bar{P}^m_n(\nu_2)\bar{Q}^m_n(\eta_2)\sin(m\psi_2))}{\partial z_1} d\xi_2 d\nu_1 d\psi_1 \tag{10}$$

Similarly, for the elements in $[L_{21}]$,

$$L^{0m}_{jn,\cos} = \frac{1}{2\pi}\int_0^{2\pi}\int_0^1 \Psi^0_j(\nu_2)* \int_0^\infty \frac{\partial(\bar{P}^m_n(\nu_1)\bar{Q}^m_n(\eta_1)\cos(m\psi_1))}{\partial z_2} d\xi_1 d\nu_2 d\psi_2 \tag{11}$$

$$L^{rm}_{jn,\cos} = \frac{1}{\pi}\int_0^{2\pi}\int_0^1 \Psi^r_j(\nu_2)\cos(r\psi_2)* \int_0^\infty \frac{\partial(\bar{P}^m_n(\nu_1)\bar{Q}^m_n(\eta_1)\cos(m\psi_1))}{\partial z_2} d\xi_1 d\nu_2 d\psi_2 \tag{12}$$

$$L^{rm}_{jn,\sin} = \frac{1}{\pi}\int_0^{2\pi}\int_0^1 \Psi^r_j(\nu_2)\sin(r\psi_2)* \int_0^\infty \frac{\partial(\bar{P}^m_n(\nu_1)\bar{Q}^m_n(\eta_1)\sin(m\psi_1))}{\partial z_2} d\xi_1 d\nu_2 d\psi_2 \tag{13}$$

As closed form expressions for these off-diagonal blocks have not yet been found, they are pre-computed and stored in a lookup table indexed by inflow skew angle. Lastly, an interference induced velocity exponential decay function[10] is used to account for viscous wake decay. The function is given as,

$$V_{decay}(d) = e^{(-d\,\zeta)} \tag{14}$$

where d is the distance of the flow field point of interest from the center of the source rotor that generates the interference and ζ is the empirical decay coefficient.

4. INFLOW DISTRIBUTION ANALYSIS

The most direct method to compare inflow distribution between different models is to plot the contour of downwash variation radially at each azimuthal step for one complete revolution of each rotor disk. While such a comparison clearly highlights the region where differences are present, it provides little quantitative information. A more commonly used approximation to quantify the effects of nonuniform inflow in forward flight is given in equation (15)[11]. The inflow across the rotor disk due to mean and cyclic loadings can be expanded up to the uniform and first harmonic terms as,

$$\bar{v}_z(\bar{r},\psi) = \lambda_0 + \lambda_{1\mathrm{c}}\bar{r}\cos(\psi) + \lambda_{1\mathrm{s}}\bar{r}\sin(\psi) \tag{15}$$

By using the orthogonal property of trigonometric functions, the inflow coefficients in equation (15) is found to be,

$$\lambda_0 = \frac{1}{\pi}\int_0^{2\pi}\int_0^1 \bar{v}_z(\bar{r},\psi)\bar{r}\,d\bar{r}\,d\psi \tag{16}$$

$$\lambda_{1\mathrm{c}} = \frac{4}{\pi}\int_0^{2\pi}\int_0^1 \bar{v}_z(\bar{r},\psi)\bar{r}^2\cos(\psi)\,d\bar{r}\,d\psi \tag{17}$$

$$\lambda_{1\mathrm{s}} = \frac{4}{\pi}\int_0^{2\pi}\int_0^1 \bar{v}_z(\bar{r},\psi)\bar{r}^2\sin(\psi)\,d\bar{r}\,d\psi \tag{18}$$

These linear inflow variation equations are related to the aerodynamic loads up to the first harmonic, but are not sufficient for detailed inflow variation studies. As such, inflow states are also used to provide a more comprehensive analysis. The main advantage of using inflow states is the additional degree-of-freedom to select the order of inflow variation across the disk. Furthermore, inflow states can be extracted from VPM inflow results using the following equations,

$$\alpha^0_n = \frac{1}{2\pi}\int_0^{2\pi}\int_0^1 \bar{P}^0_n(\bar{r})\bar{v}_z(\bar{r},\psi)\bar{r}\,d\bar{r}\,d\psi \tag{19}$$

$$\alpha^m_n = \frac{1}{\pi}\int_0^{2\pi}\int_0^1 \bar{P}^m_n(\bar{r})\bar{v}_z(\bar{r},\psi)\bar{r}\cos(m\psi)\,d\bar{r}\,d\psi \tag{20}$$

$$\beta^m_n = \frac{1}{\pi}\int_0^{2\pi}\int_0^1 \bar{P}^m_n(\bar{r})\bar{v}_z(\bar{r},\psi)\bar{r}\sin(m\psi)\,d\bar{r}\,d\psi \tag{21}$$

Therefore, the inflow coefficients and inflow states defined in equations (16) through (21) are used in this study for comparison of inflow predictions of a coaxial rotor system using the ARRIM and the VPM.

5. SIMULATION SETUP

The geometric and aerodynamic data for the Harrington coaxial rotor[5] has been used in developing an isolated coaxial rotor model in FLIGHTLAB®. Both upper and lower rotors have a diameter of 25 feet with separation distance of 2.375 feet (19 percent of rotor radius) between the rotors. The blades are untwisted and have linearly tapered chord from 12.5 inches at the root to 4 inches at the tip. While Ref. 5 did not describe specific airfoils used for the rotors in the experiment, it is mentioned that NACA four-digit symmetrical airfoil sections were used for the blades. As such, the current model uses airfoils from the four-digit series that roughly match the actual

blade's thickness distribution. From the root up to 60 percent of the blade radius, NACA 0026 airfoil table is used while the remaining segment of the blade is modeled using NACA 0012. In order to account for the observed contour defects of the blades in the experiment, measured blade drag polar is used in the analysis report by Dingeldein[6]. Since the drag polar data is not available in both Refs. 5 and 6, a constant drag polar bias is used in the current model to adjust the torque coefficient curve such that a single rotor at zero collective matches experimental data in hover.

The default finite-state inflow model in FLIGHTLAB® is disabled and replaced by ARRIM to provide inflow calculations. The ARRIM is integrated into the flight model as an external module that takes the blade loadings from FLIGHTLAB®'s aerodynamic component as input illustrated in Fig. 1. At a given control setting, the rotor blades' lift distribution at the aerodynamic computation points (ACP) are stored for one complete rotor revolution and are used to compute the average pressure coefficients. From the pressure coefficients, the inflow states are iterated until they achieve convergence as shown in "Iteration A" in Fig. 1. With the converged inflow states, induced downwash over the upper and lower rotor disks are obtained using equation (3). The ARRIM module outputs these inflow distributions to each rotor's aerodynamic model to update the lift forces on the blades. In FLIGHTLAB®, the loop between ARRIM and the blades' aerodynamic component shown as "Iteration B" in Fig. 1 is iterated until convergence of rotor lift and inflow distributions.

FLIGHTLAB® trimming algorithm is used to trim the coaxial rotor model in hover and forward flight. The algorithm perturbs the control settings and iterates the ARRIM-aerodynamic component loop until steady-state is obtained. It then calculates the corresponding performance values such as the rotor's thrust coefficient, torque coefficient and horizontal force. If these computed values match the target settings within a given tolerance, the algorithm will determine that the model has achieved trim and outputs the control settings along with the computed performance values.

In hover mode, the collective settings of upper and lower rotors are adjusted so that total thrust generated matches selected value of thrust coefficient with zero net torque. The trimmed collective settings for upper and lower rotors are presented in Fig. 2, with the lower rotor (circle markers) requiring higher collective settings as compared to upper rotor as expected. A breakdown of thrust produced by each rotor shown in Fig. 3 further illustrates that the lower rotor is less effective in thrust generation; a characteristic of coaxial rotor configuration in hover. Finally, the hover trim torque predictions from FLIGHTLAB® for varying thrust coefficients correlate well with experimental data in Fig. 4.

For forward flight, the coaxial rotor model is trimmed by adjusting the collective and longitudinal cyclic controls of the upper and lower rotors. The lateral cyclic of both rotors are set to zero and longitudinal cyclic control of lower rotor is set to be equal to that of the upper rotor. The steady-state trim targets are the total vertical force which balances specified total thrust coefficient of 0.0048 and total horizontal force is trimmed to balance the parasite drag associated with a flat plate area of 10 square-feet as specified in Ref. 6. The upper and lower rotor torque values are also trimmed to balance each other. The predicted trim control settings are shown in Fig. 5 with the collective and longitudinal cyclic following expected trends in forward flight. The variation of power required prediction from ARRIM in FLIGHTLAB® is also compared with experimental data in Fig. 6. At all advance ratios, ARRIM underestimates power requirements similar to what was reported in the literature using ARRIM implemented in RCAS[12].

6. ARRIM AND VPM INFLOW DISTRIBUTION COMPARISON

A physics-based CFD model such as the VPM is used to generate inflow distributions for the Harrington teetering coaxial rotor in FLIGHTLAB®. The vorticity sources are created from individual rotor blade ACPs and are released into the flow field. The VPM then solves the vorticity equation in a global reference which automatically captures the upper and lower rotor mutual interferences. The same set of ACPs corresponding to upper and lower rotor blades are used for both the VPM and ARRIM.

Flow fields corresponding to hover and advance ratios of 0.15 and 0.25 are used for comparison between the ARRIM and the VPM. The inflow distribution up to first harmonics are shown in Figs. 7, 8 and 10. In hover, only the uniform inflow is present while other harmonics are very close to zero as shown in Fig. 7. There is also little difference between mean inflow predicted by VPM and by ARRIM. This is expected since the upper rotor wake is almost cylindrical, albeit some contraction effects which is well captured by ARRIM.

At advance ratio of 0.15 shown in Fig. 8, the ARRIM over-estimates mean inflow by 27% and 36% for the upper and lower rotors, respectively. Differences in λ_{1c} is more significant, especially at the lower rotor. A qualitative comparison of the inflow distribution

between VPM and ARRIM predictions at advance ratio of 0.15 is presented in Fig. 9. Notice that for VPM upper and lower rotor inflow distributions, there is upwash occurring at an arc region sweeping from the advancing to retreating side. On the other hand, ARRIM predicts that upwash is only present near the front part of both rotors. An interesting observation for the advance ratio of 0.25 is the presence of side-to-side inflow gradient from VPM results as shown in Fig. 10. This means that the near symmetrical inflow distribution about the longitudinal axis seen for the lower advance ratio of 0.15 case is not found at the higher advance ratio of 0.25 case as illustrated in Fig. 11. VPM predicts that a region of upwash is concentrated only at one quadrant of each rotor disk. In addition, there are small pockets of high downwash content distributed across upper and lower rotor disks in the VPM results. On the the other hand, ARRIM shows that significant downwash only occurs at the aft region of both rotors.

The upper and lower rotor wake skew angles computed by ARRIM are also compared with the VPM results in Fig. 12. There is no major difference in terms of wake skew angles between these two models. As noted from the study conducted by Kim et al.[13] on Harrington coaxial rotor using vorticity transport model (VTM), it is reported that the wake skew angles for a coaxial system is comparable to equivalent single rotor system at all advance ratios. Since ARRIM is formulated assuming cylindrical wake (similar to single rotor system), it is not surprising to find the wake skew angle differences between ARRIM and VPM to be insignificant.

The inflow states extracted from VPM inflow predictions are compared with ARRIM predictions in Figs. 13 through 15. A 10-state ARRIM is used for comparison because there is no significant difference in terms of trim control settings between 10-state and 28-state ARRIM. In addition, the 10-state ARRIM is used so that sufficiently high harmonics are analysed without cluttering the plots with too many states.

Hover inflow states are shown in Fig. 13 with only zeroth-harmonics present in the chart. Similar to the linear inflow distribution comparisons discussed earlier, ARRIM prediction for the first uniform inflow state is comparable to VPM results. For advance ratio of 0.15 results shown in Fig. 14, there are large differences between the two models, especially for the longitudinal cosine components. For advance ratio of 0.25 shown in Fig. 15, non-zero values of sine components of inflow states in VPM results are observed as well.

From the inflow distribution analysis of the upper and lower rotors, it is observed that the uniform inflow is somewhat similar to the VPM results. However, the longitudinal and lateral inflow gradients predicted by ARRIM are quite different from the VPM results. Appropriate downwash corrections can be applied at each ACP by using the delta-form of equation (3). But this correction is only of first-order fashion which may not be sufficient to match the complicated inflow distribution in forward flight. By computing the differences in inflow states between ARRIM and VPM results, correction terms can be augmented into the ARRIM using the mass-flow parameter and L-matrix. For dynamic inflow conditions, corrections to the apparent mass matrix may have to be taken into consideration as well.

7. CONCLUSION

A previously developed finite state Active-Receiving Rotor Inflow Model (ARRIM) has been implemented in FLIGHTLAB®. In order to gain an insight into the ability of ARRIM to predict the complex nature of inflow of a coaxial rotor system, the ARRIM predictions are compared with those using the Vortex Particle Model (VPM) from the literature. The VPM is a physics-based CFD model that captures both vorticity stretching and vorticity diffusion due to air viscosity.

The inflow distributions for upper and lower rotors of the Harrington coaxial rotor system are obtained in hover and at two advance ratios. The uniform, and the first harmonic components of inflow predictions from ARRIM are compared with those using the VPM.

Both models are seen to predict nearly the same mean inflow in hover with very little harmonic content. At advance ratio of 0.15, the upper and lower rotor mean inflow predictions from ARRIM are slightly above the mean inflow predictions from VPM. However, the fore-to-aft inflow gradient prediction from 10-state ARRIM is seen to be as much as 114% more than that from VPM. At higher advance ratio of 0.25 case, side-to-side inflow content is observed in VPM results where such content is absent in the ARRIM results.

This study has identified the primary differences in inflow predictions of a coaxial rotor system in forward flight between ARRIM and VPM. The next step is to arrive at appropriate corrections to the parameters of the ARRIM in order to improve its correlations with a high fidelity model such as VPM or a free-wake model. It is expected that this forms an important step for improving ARRIM correlations with the very limited and mostly performance related coaxial rotor data available in the literature.

8. ACKNOWLEDGMENTS

The authors would like to thank Dr. Hong Xin of Sikorsky Aircraft Corp. for his comments and feedback in this study.

This study is supported under the NRTC Vertical Lift Rotorcraft Center of Excellence (VLRCOE) from the U.S. Army Aviation and Missile Research, Development and Engineering Center (AMRDEC) under Technology Investment Agreement W911W6-06-2-0002, entitled National Rotorcraft Technology Center Research Program. The authors would like to acknowledge that this research and development was accomplished with the support and guidance of the NRTC. The views and conclusions contained in this document are those of the authors and should not be interpreted as representing the official policies, either expressed or implied, of the AMRDEC or the U.S. Government. The U.S. Government is authorized to reproduce and distribute reprints for Government purposes notwithstanding any copyright notation thereon.

9. REFERENCES

[1] He, C., *Development and application of a generalized dynamic wake theory for lifting rotors*. PhD thesis, Georgia Institute of Technology, July 1989.

[2] Advanced Rotorcraft Technology, Inc., Sunnyvale, CA 94085, *FLIGHTLAB X-Analysis user manual*, July 2013.

[3] US Army Research, Develompment, and Engineering Command, Moffett Field, CA 94035-1000, *Rotorcraft Comprehensive Analysis System user's manual*, Aug. 2012.

[4] Prasad, J. V. R., Nowak, M., and Xin, H., "Finite state inflow models for a coaxial rotor in hover," in *Proceedings of the 38th European Rotorcraft Forum*, Amsterdam, Netherlands, Sept. 2012.

[5] Harrington, R., "Full scale tunnel investigation of the static thrust performance of a coaxial helicopter rotor," Tech. Rep. TN 2318, NACA, Mar. 1951.

[6] Dingeldein, R., "Wind tunnel studies of the performance of multirotor configurations," Tech. Rep. TN 3226, NASA, Aug. 1954.

[7] Zhao, J. and He, C., "A viscous vortex particle model for rotor wake and interference analysis," *Journal of the American Helicopter Society*, vol. 55, pp. 389–414, Jan. 2010.

[8] He, C. and Zhao, J., "A real time finite state induced flow model augmented with high fidelity viscous vortex particle simulation," in *Proceedings of the AHS 64th Annual Forum*, Montréal, Québec, May 2008.

[9] Zhao, J. and He, C., "Real time simulation of coaxial rotor configurations with combined finite state dynamic wake and VPM," in *Proceedings of the AHS 70th Annual Forum*, Montréal, Québec, May 2014.

[10] He, C., Xin, H., and Bhagwat, M., "Advanced rotor wake inteference modeling for multiple aircraft shipboard landing simulation," in *American Helicopter Society 59th Annual Forum*, Baltimore, MD, 2004.

[11] Wayne, J., *Rotorcraft Aeromechanics*. Cambridge University Press, 2013.

[12] Nowak, M., Prasad, J. V. R., and Peters, D., "Development of a finite state model for a coaxial rotor in forward flight," in *Proceedings of the AHS 70th annual Forum*, Montréal, Québec, May 2014.

[13] Kim, H. W. and Brown, R. E., "A comparison of coaxial and conventional rotor performance," *Journal of the American Helicopter Society*, vol. 55, p. 12004, Jan. 2010.

10. FIGURES

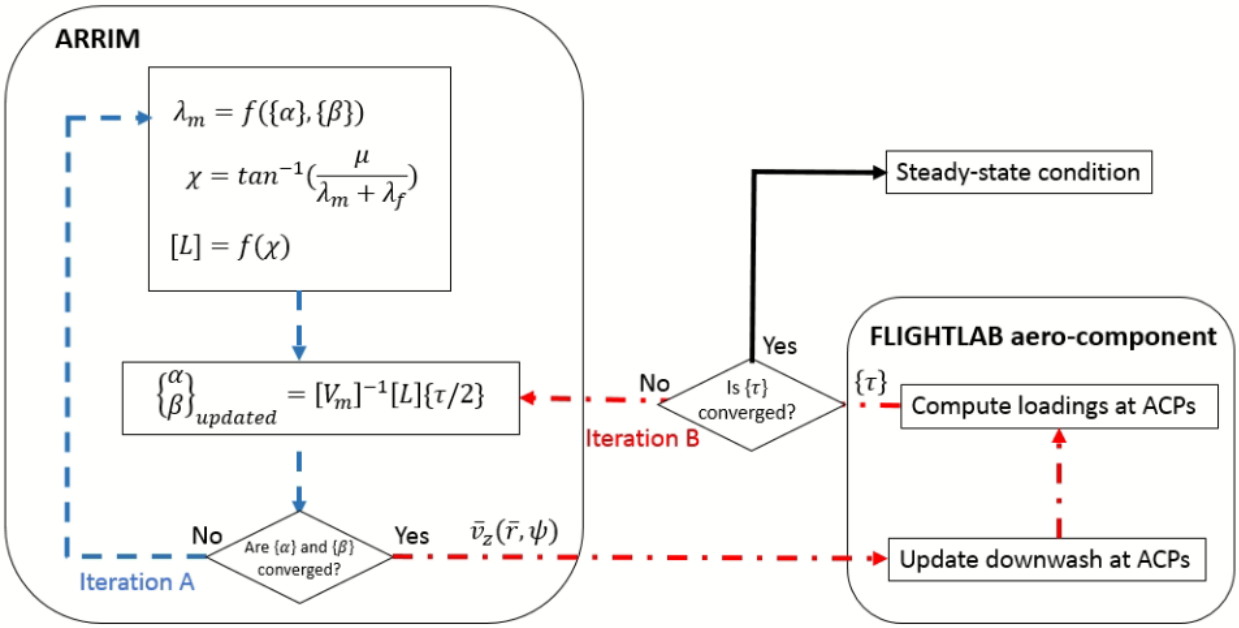

Figure 1: Simplified flow-chart of coupling between ARRIM and FLIGHTLAB®'s aerodynamic component

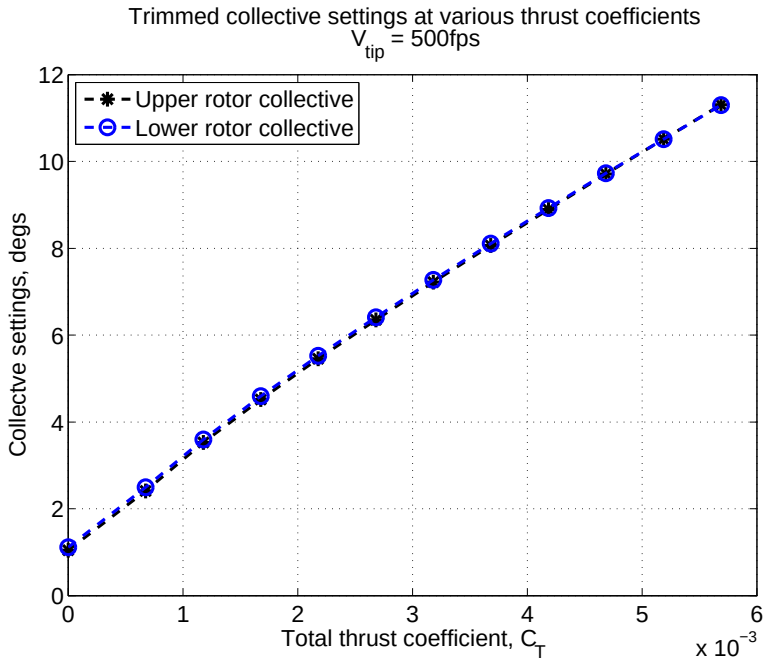

Figure 2: FLIGHTLAB® with ARRIM trim collective settings at different thrust coefficients in hover.

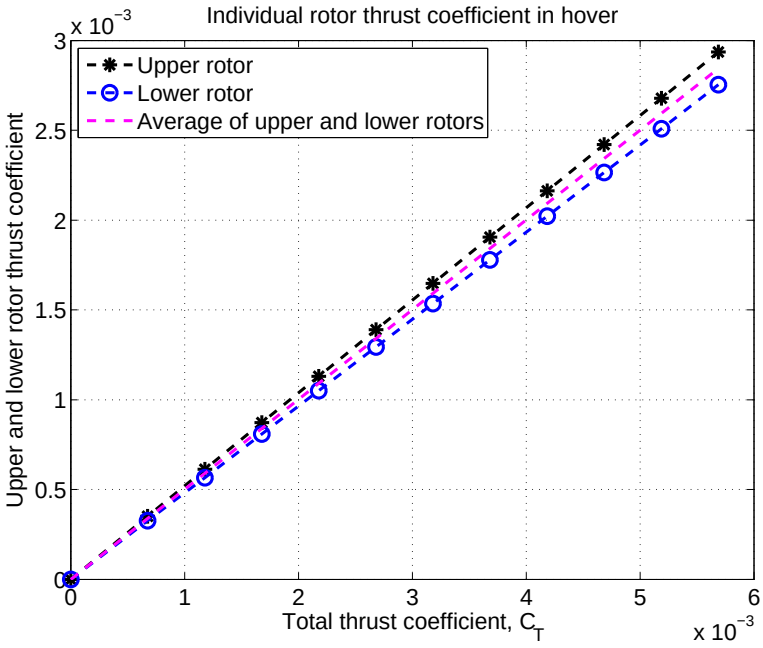

Figure 3: Thrust coefficients of upper and lower rotors in hover.

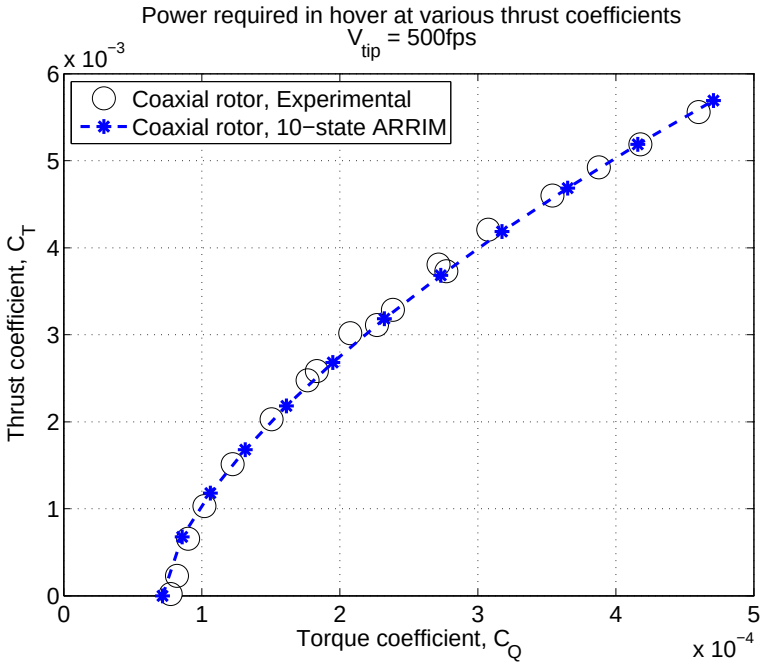

Figure 4: Correlation of FLIGHTLAB® ARRIM prediction of thrust versus torque with experimental data in hover.

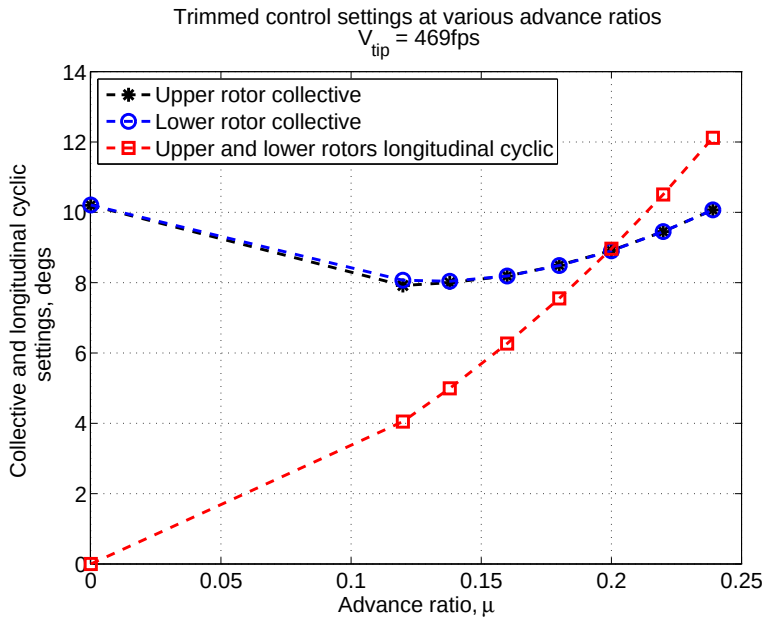

Figure 5: FLIGHTLAB® trimmed control settings for forward flight.

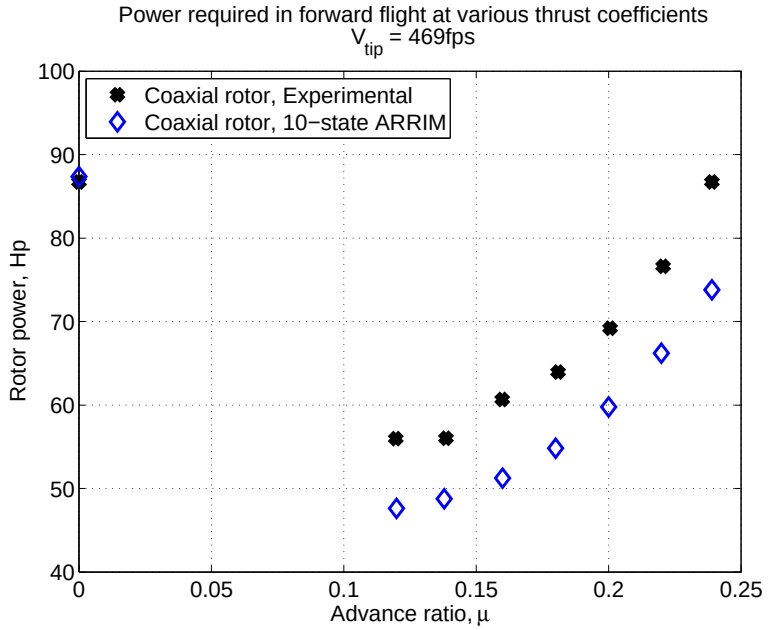

Figure 6: Correlation of FLIGHTLAB® ARRIM prediction of coaxial rotor power with experimental data in forward flight.

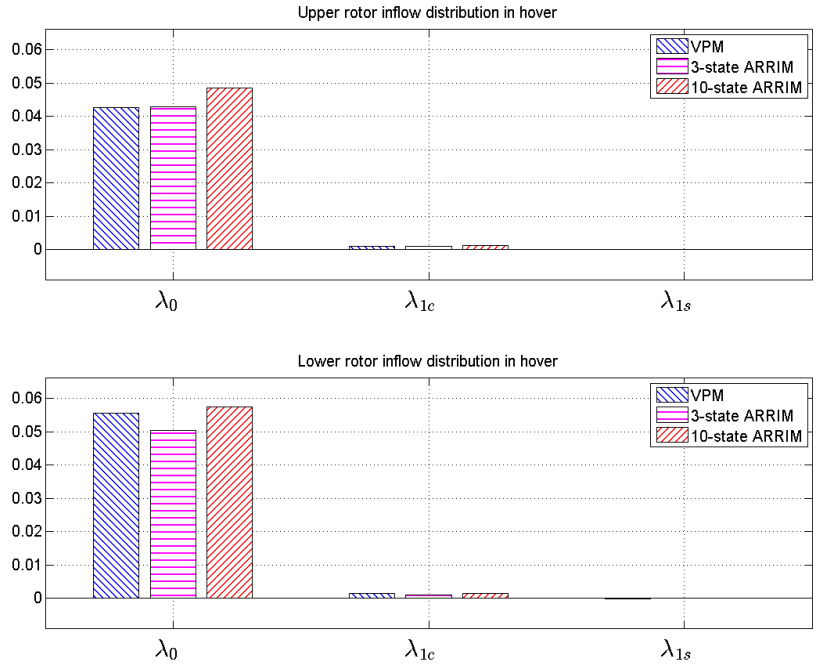

Figure 7: Comparison of mean, longitudinal and lateral inflow gradients between ARRIM and VPM predictions in hover.

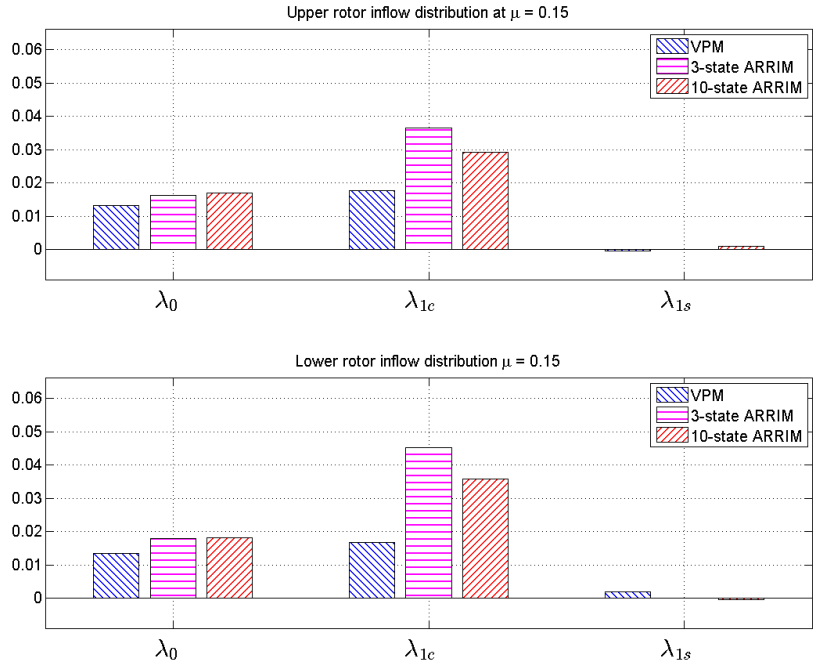

Figure 8: Comparison of mean, longitudinal and lateral inflow gradients between ARRIM and VPM predictions in forward flight (advance ratio = 0.15).

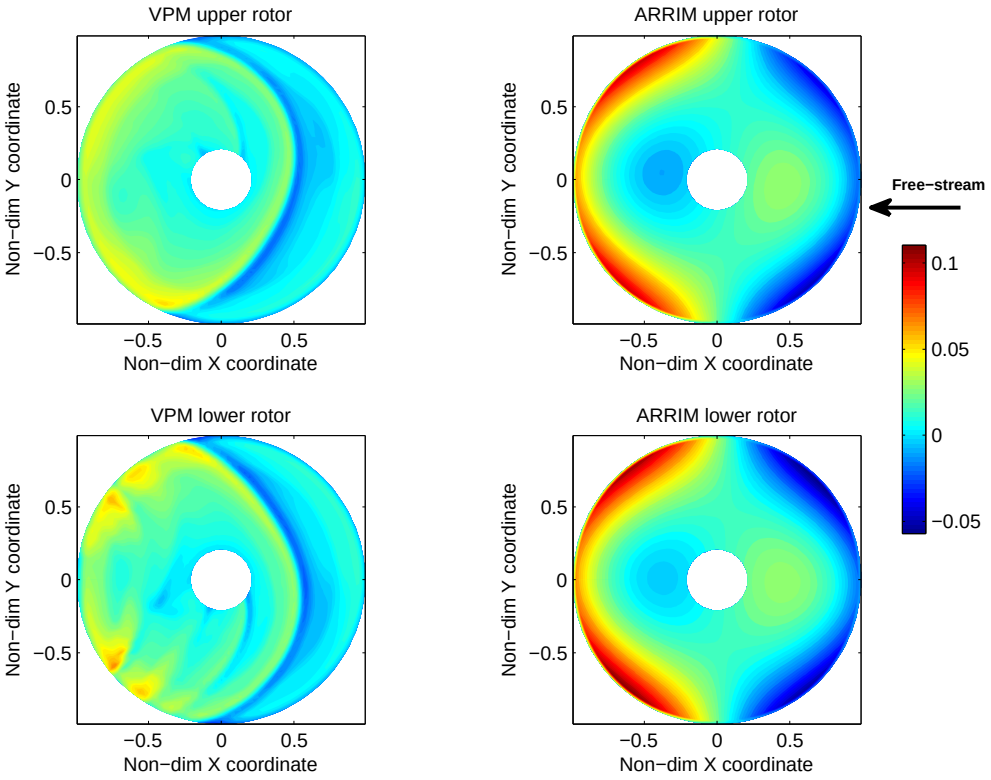

Figure 9: VPM and 10-state ARRIM inflow distribution predictions at advance ratio of 0.15. The upper rotor rotates clockwise and lower rotor rotates counter-clockwise when viewed from the top.

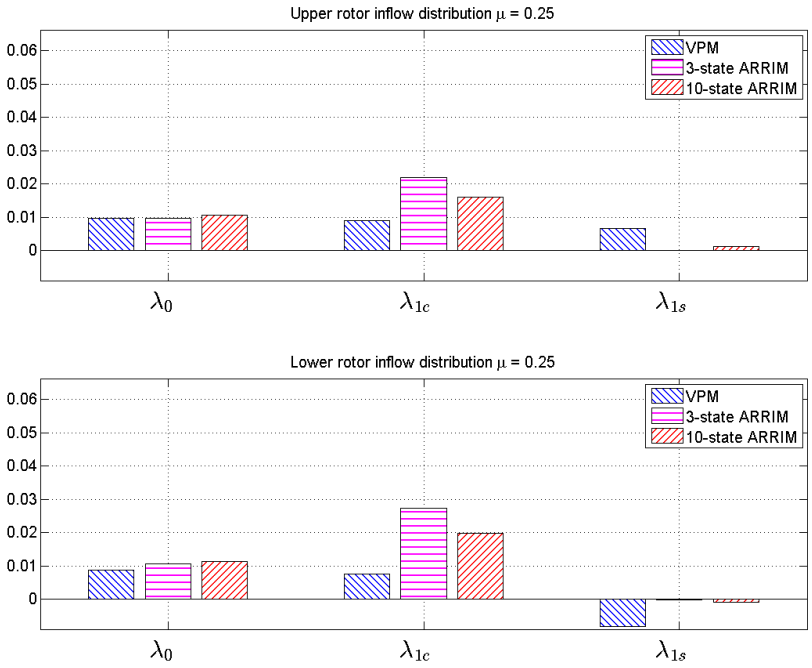

Figure 10: Comparison of mean, longitudinal and lateral inflow gradients between ARRIM and VPM predictions in forward flight (advance ratio = 0.25).

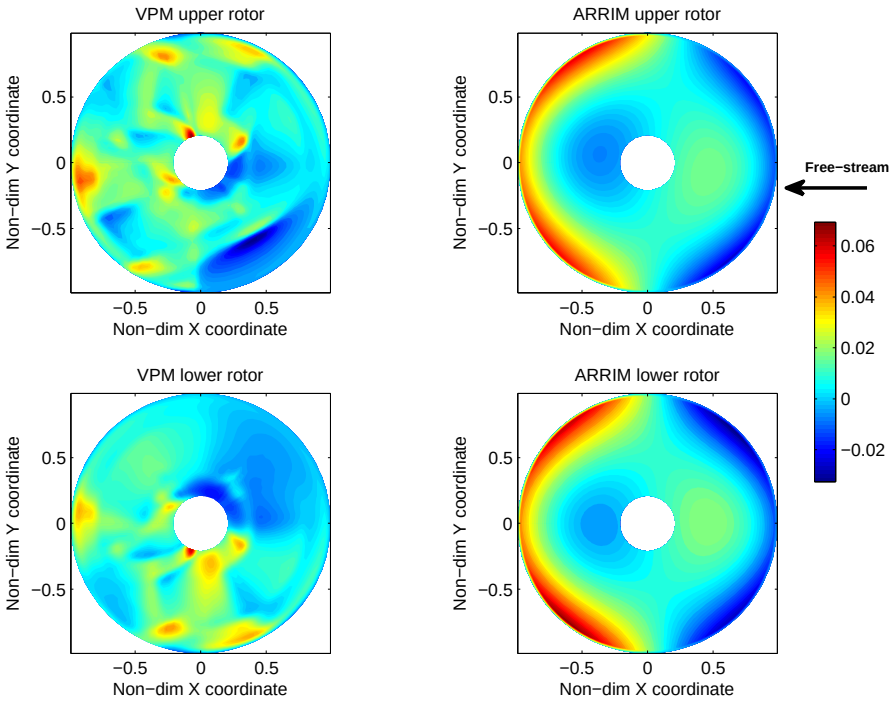

Figure 11: VPM and 10-state ARRIM inflow distribution predictions at advance ratio of 0.25. Presence of significant upwash occurring only on one side of each rotor disk contributing to side-to-side inflow gradient in VPM results.

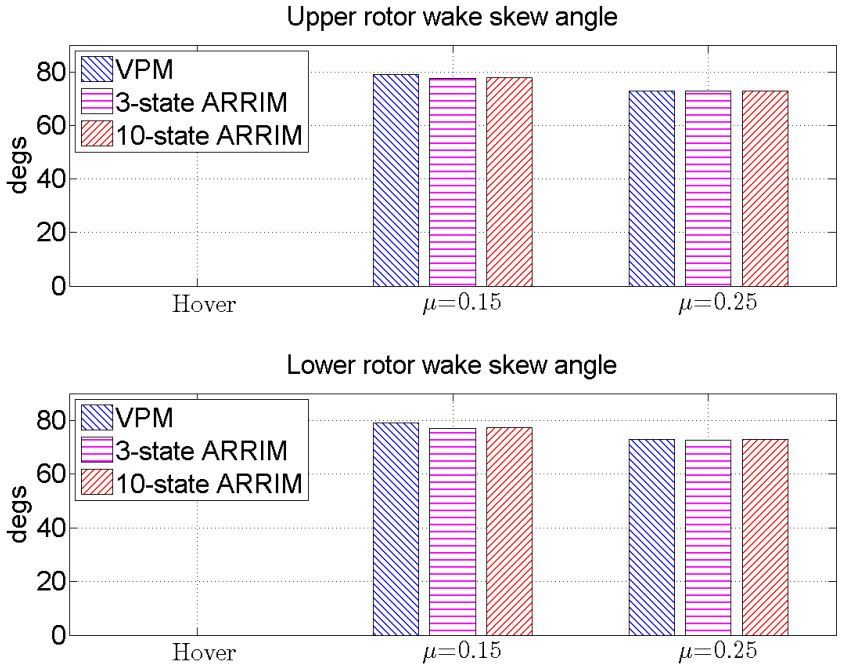

Figure 12: Upper and lower rotor wake skew angles.

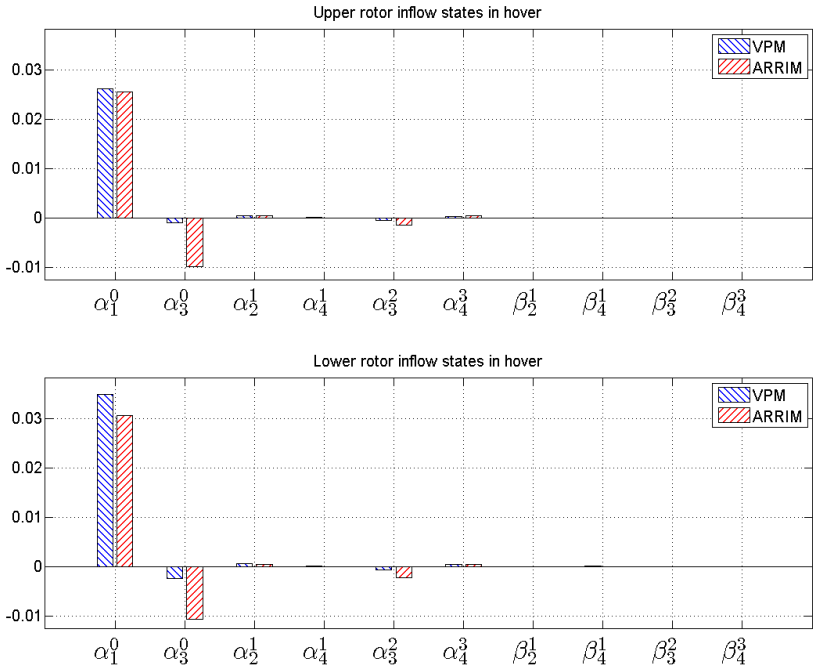

Figure 13: Comparison of upper and lower rotor inflow states between VPM and 10-state ARRIM in hover.

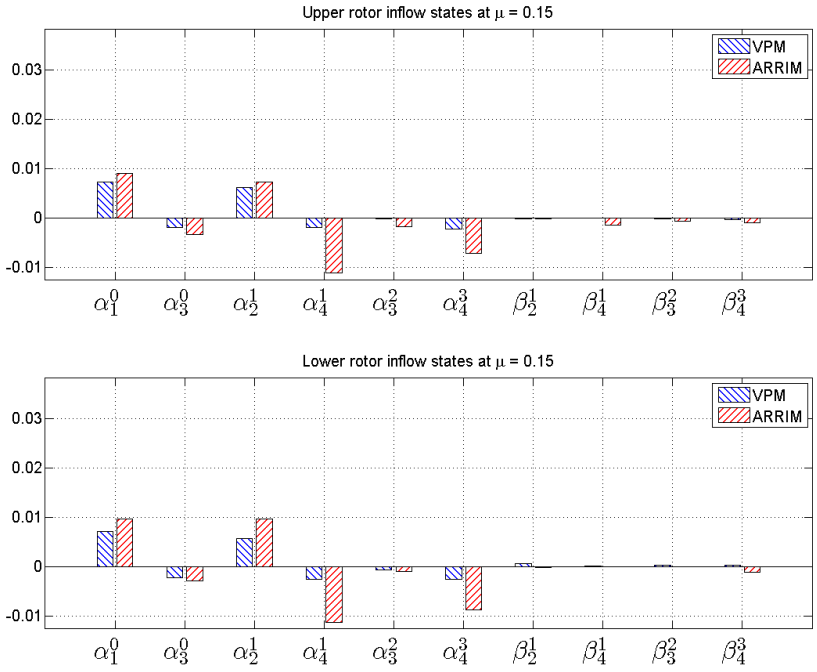

Figure 14: Comparison of upper and lower rotor inflow states between VPM and 10-state ARRIM at advance ratio of 0.15.

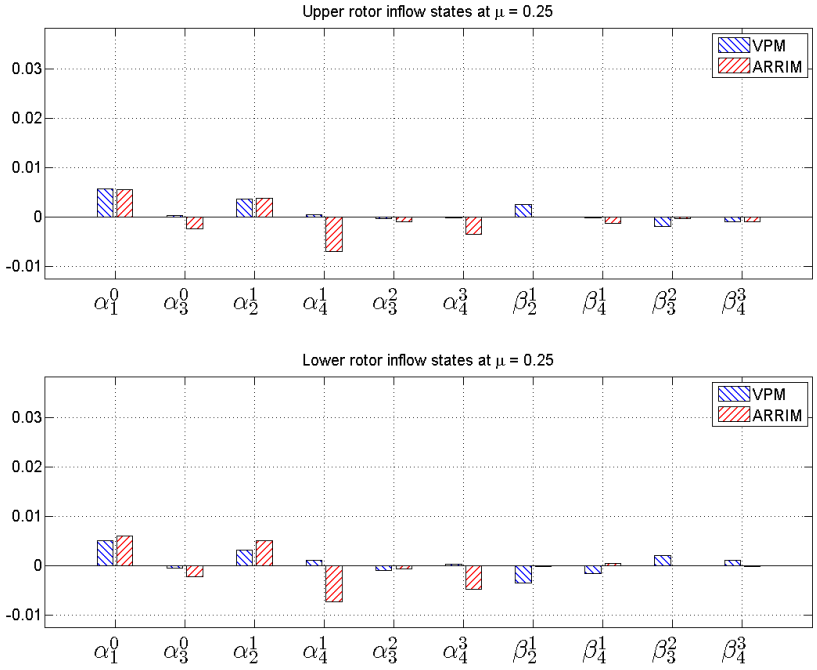

Figure 15: Comparison of upper and lower rotor inflow states between VPM and 10-state ARRIM at advance ratio of 0.25.